Convection in Slab and Spheroidal Geometries

David H. Porter, Paul R. Woodward, and Michael L. Jacobs

Laboratory for Computational Science and Engineering
University of Minnesota
116 Church St. S.E.
Minneapolis MN 55455, USA

Abstract.

Three-dimensional numerical simulations of compressible turbulent thermally driven convection, in both slab and spheroidal geometries, are reviewed and analyzed in terms of velocity spectra and mixing length theory. The same ideal gas model is used in both geometries, and resulting flows are compared. The Piecewise-Parabolic Method (PPM), with either thermal conductivity or photospheric boundary conditions, is used to solve the fluid equations of motion.

Fluid motions in both geometries exhibit a Kolmogorov-like $k^{-5/3}$ range in their velocity spectra. The longest wavelength modes are energetically dominant in both geometries, typically leading to one convection cell dominating the flow. In spheroidal geometry, a dipolar flow dominates the largest scale convective motions. Downflows are intensely turbulent and updrafts are relatively laminar in both geometries. In slab geometry, correlations between temperature and velocity fluctuations, which lead to the enthalpy flux, are fairly independent of depth. In spheroidal geometry this same correlation increases linearly with radius over the inner 70 percent by radius, in which the local pressure scale heights are a sizable fraction of the radius. The effects from the impenetrable boundary conditions in the slab geometry models are confused with the effects from non-local convection. In spheroidal geometry non-local effects, due to coherent plumes, are seen as far as several pressure scale heights from the lower boundary and are clearly distinguishable from boundary effects.

Proceedings of the Fourteenth International Annual Florida Workshop in Nonlinear Astronomy and Physics, "Astrophysical Turbulence and Convection," University of Florida, Feb. 1999
(to appear in the Annals of the New York Academy of Sciences)

1. Introduction

Many stars, including our Sun as well as red giants, are expected to have convective envelopes which span many pressure scale heights, in which efficient convective mixing is expected to produce a nearly adiabatic radial profile. Near the bases of these convection zones the amplitude, distribution, and coherence of turbulent convective motions is expected to determine the extent of penetra-

tion and mixing into the stable region below. In the uppermost pressure scale heights, the distribution of convectively driven motions affects the mean radial profile as well as the size of granules, or even star spots, on the surface.

Here, we use well resolved 3-D numerical simulations to study the influence of global geometry on the distribution and statistics of fluctuating fluid variables in thermally driven compressible convection. In these systems a wide range of length scales are directly modeled and seen to interact. We are interested in the velocity spectrum of these convective flows as an example of fully developed anisotropic turbulence driven by a wide range of scales. We also wish to examine issues pertinent to variants of Mixing-Length Theory (MLT), both local and non-local, in terms of the amplitudes and correlations of fluctuating fluid dynamic quantities. Previous studies of thermally driven convection in slab geometry have shown velocity spectra which possess a $k^{-5/3}$ Kolmogorov-Obukhov like range (Chan and Sofia 1989, Cattaneo et. al. 1991, Porter and Woodward 2000) and have examined a wide variety of statistical measures (Chan and Sofia 1989, Singh and Chan 1993, Chan and Sofia 1996, Kim et. al. 1996, and Porter and Woodward 2000). Axially symmetric 2-D numerical models of radially deep sectors have also been used to test mixing length parameters relevant to red giant envelopes (Asida and Tuchman 1997, and Asida 2000).

We model an ideal inviscid gas in a gravitational field $\mathbf{g}$ with radiative diffusivity χ, nuclear heating S_{nuc}, and photospheric cooling S_{photo}. In terms of the independent variables of space $\mathbf{X}$ and time t, we follow the fluid variables of mass density ρ, pressure P, fluid velocity $\mathbf{u}$. The equations of motion are based on conservation of mass

$$\partial_t \rho + \nabla \cdot (\rho \mathbf{u}) = 0 \quad , \tag{1}$$

momentum

$$\partial_t \mathbf{u} + \mathbf{u} \cdot \nabla \mathbf{u} = -\frac{\nabla P}{\rho} + \mathbf{g} \quad , \tag{2}$$

and energy

$$\partial_t (\rho E) + \nabla \cdot (\mathbf{u} \rho E) = -\nabla \cdot (\mathbf{u} P - \chi \nabla T) + S_{nuc} - S_{photo} \quad , \tag{3}$$

where the energy density per unit mass is $E = \frac{1}{2}\mathbf{u}^2 + \epsilon + \phi$. Here, ϕ is the gravitational potential which is related to the local acceleration due to gravity in the usual way $\mathbf{g} = -\nabla\phi$. The equation of state is that of a polytropic γ-law gas $P = (\gamma - 1)\rho\epsilon$, where the internal energy is related to the temperature via the specific heat at constant volume $\epsilon = c_v T$.

In the slab convection models, impenetrable boundaries are imposed at top and bottom, and the thermal diffusivity χ and acceleration due to gravity, $\mathbf{g}$ are both constant. A constant energy flux is imposed along the lower boundary, and a constant temperature is imposed long the top, while the heating and cooling terms S_{nuc} and S_{photo} are zero. In the spheroidal geometry models $\mathbf{g}$ is radial in direction and a function of the total mass within the local radius. The thermal diffusivity is minimal (in some of the models the radiative flux is negligible in the interior) and the energy flux is imposed by injection of heat, via the S_{nuc} near the impenetrable core. The photospheric cooling term S_{photo} takes

the form $\sigma T^4 |\nabla e^{-\tau}|$, where τ is an estimate of the local optical depth given by $(\rho/\rho_o)^n$. S_{photo} is only non-zero near the surface, where $\tau \approx 1$. This cooling term imposes a photospheric boundary condition, where the cooling per unit area goes as σT^4. At the radial lower boundary, a spherical impenetrable region is imposed on the mesh. Convection in both geometries is solved on a Cartesian mesh via the Piecewise Parabolic Method (Woodward and Colella 1984, Colella and Woodward 1984, Woodward 1986).

2. Convection in Slab Geometry

Results from a numerical simulation of thermally driven convection in slab geometry are reviewed here in order to contrast them with results from spheroidal geometry models. The volume simulated is 2x2x1 in aspect ratio, on a mesh resolution of 512x512x256, and periodic in both horizontal directions. Free slip impenetrable walls are imposed along the top and bottom boundaries. The vertical dimension spans five pressure scale heights. Here, the focus is on simulations of efficient convection: in this model the thermal diffusivity carries 8% of the total energy flux. Comparisons with inefficient convection, and tests of convergence with computational mesh resolution, are reviewed in Porter and Woodward 2000.

Fig. 1 shows temperature fluctuations relative to the horizontal mean at each depth. Only cool fluctuations are shown, warm temperature fluctuations are relatively laminar and are rendered transparent. Fig. 2 shows the magnitude of vorticity in a vertical section. The strongest vorticity is found in the downflow lanes, both near the top boundary and throughout the volume.

Peak convective Mach numbers range from 0.2 near the lower boundary to nearly unity along the top in this model. The increase of Mach number with height is primarily due to the decreasing sound speed with height. Velocity fluctuations increase with height, but only slightly. The left panel in Fig. 3 shows a comparison of the *rms* radial (or vertical in slab geometry) velocity fluctuations from the 3D simulation (solid line) compared with a dimensional analysis based on the kinetic energy flux (dashed line).

$$\delta U_R = \left(\frac{2 F_{C,est}}{\rho} \right)^{1/3} \tag{4}$$

Since 8% of the imposed total energy flux is carried by radiation in this model, the estimated convective flux $F_{C,est}$ is set to be 92% of the imposed flux along the lower boundary. Agreement between the estimated velocity fluctuations and those from the 3D simulation are surprisingly good except near the top and bottom, where the hard wall boundaries constrain the radial velocity to go to zero.

The spectrum of the radial/vertical velocity taken in a horizontal section at Z=0.5 (mid depth), shown in the right panel of Fig. 3, possesses a Kolmogorov-like power-law range from $k/k_{min} = 1$ to $k/k_{min} = 16$. The spectrum of velocity fluctuations is energetically dominated by the lowest modes, and the $k^{-5/3}$ range starts at $k/k_{min} = 1$. The dominance of the fundamental horizontal mode is

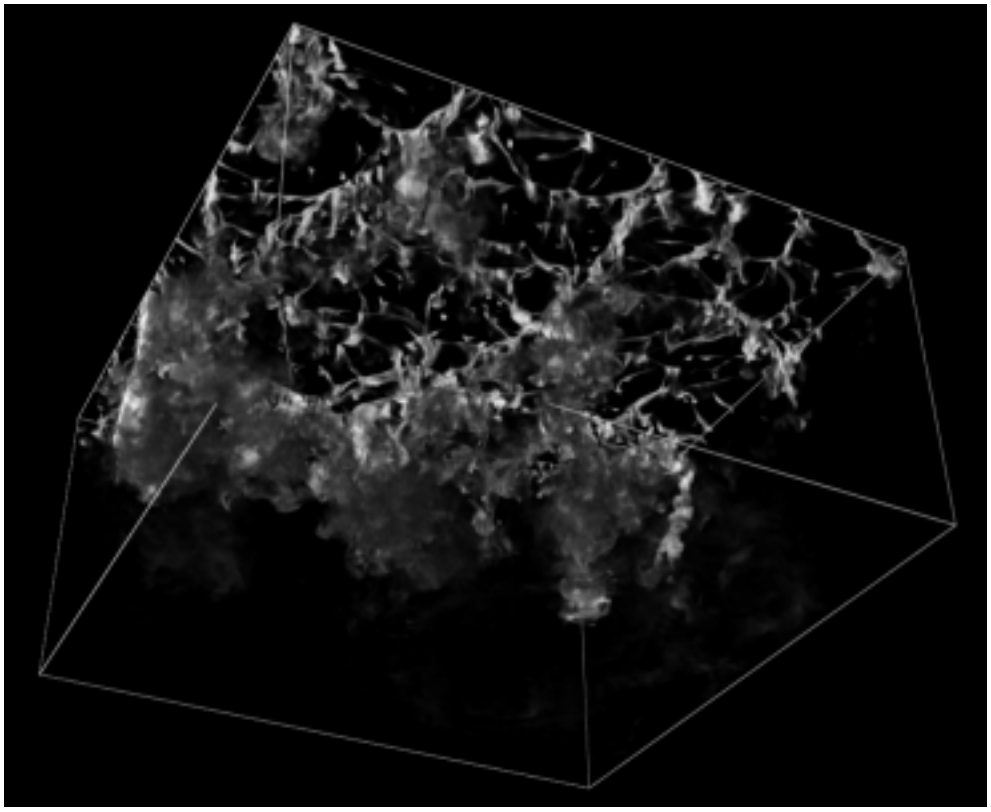

Figure 1. Temperature fluctuations relative to the horizontal mean from a simulation of slab convection. Only cool fluctuations are shown.

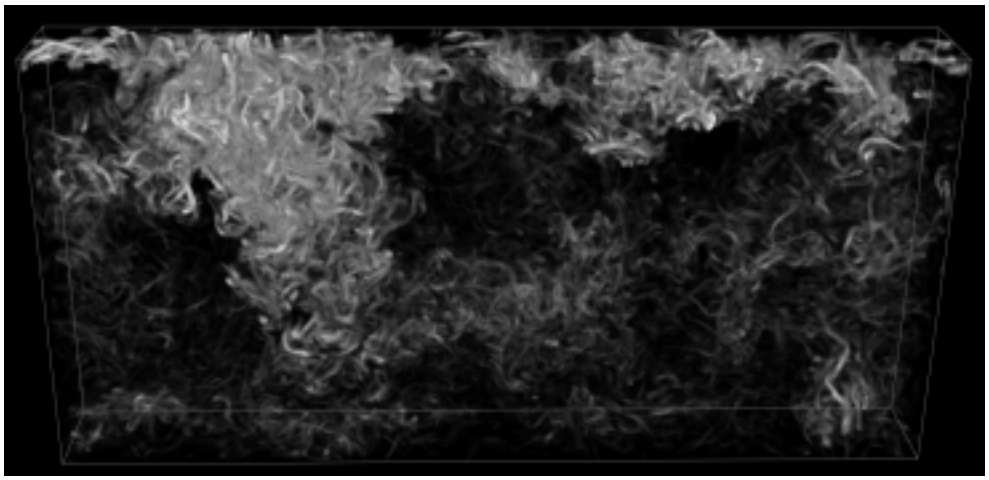

Figure 2. Vortex tubes in a slice from a simulation of convection in slab geometry.

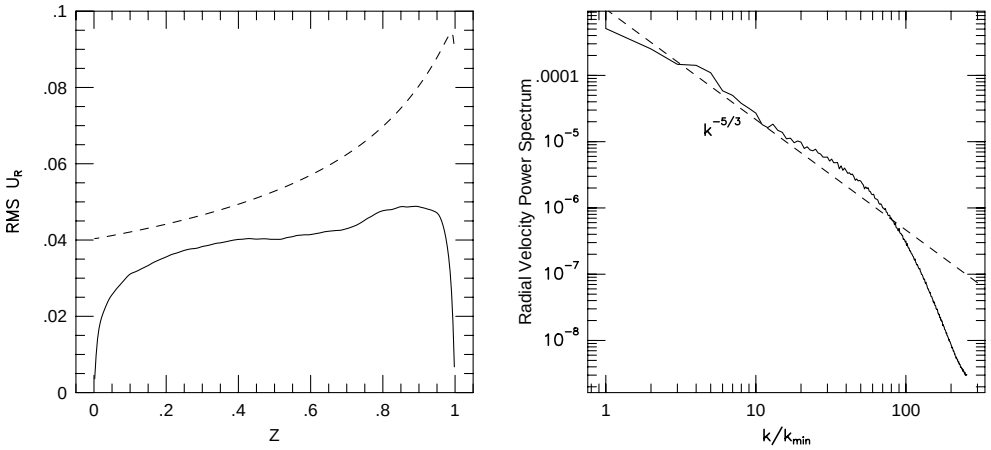

Figure 3. Radial velocity fluctuations (left) and radial velocity power spectra in a horizontal section (right).

also seen in the visualizations in Fig. 1 and Fig. 2 : one convection cell fills the horizontal extent of the model in the lowest pressure scale height.

As has been been seen in simulations of isotropic homogeneous turbulence using PPM (Porter et. al. 1994), there is a bump, or excess over the $k^{-5/3}$ scaling in the near dissipation range, which spans $k_{max}/k = [4, 16]$. Given the mesh resolution, this range of wavenumbers corresponds to spatial displacements from $4\Delta x$ to $16\Delta x$. This bump is also seen in Naiver-Stokes models of homogeneous decaying turbulence (Sytine et. al. 1999) and is believed to correspond to a bottleneck in the forward transfer of energy (Porter et. al. 1994, and Lohse and Muller-Groeling 1995).

2.1. Local MLT in Slab Geometry

Radial profiles of stellar atmospheres are commonly modeled by assuming hydrostatic equilibrium and estimating a local temperature gradient based on the local convective energy flux and some variant of MLT. Given the large scale convective plumes and dominance of large wavelength modes seen in the slab convection model discussed above, non-local effects are inevitable in relating the velocity and temperature fluctuations to the vertical profile of the atmosphere. However, evaluation of the correlation coefficients related to a local MLT is still illuminating, especially when compared to those from convection in spheroidal geometry. Surprisingly, a very simple local MLT model fits the scalings of the data from the slab convection model quite well. Fig. 4, left panel, shows the average logarithmic temperature gradient $\nabla = \partial lnT/\partial lnP$, as a function of Z, from the model of efficient convection in slab geometry reviewed above. Given the $\gamma = 5/3$ ideal gas, an adiabatic atmosphere would have a logarithmic temperature gradient of $\nabla_{ad} = 0.4$, which is shown as a dotted line in Fig. 4. There is a subadiabatic temperature gradient in the lowest pressure scale height due to a combination of the the impenetrable wall at the bottom and non-local effects. The temperature gradient is superadiabatic in the upper pressure scale heights, and becomes increasingly superadiabatic as Z increases.

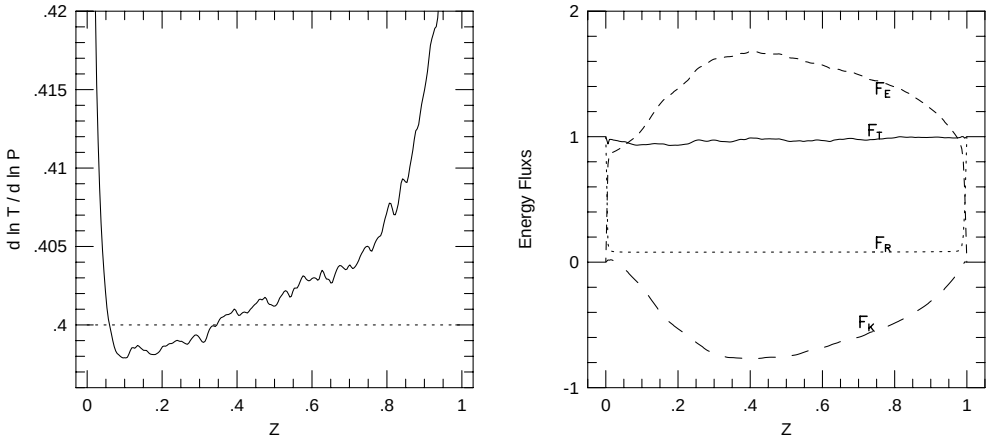

Figure 4. Logarithmic temperature gradient (left) and components of the energy flux (right) as functions of height in slab convection.

Fig. 4, right panel, shows the enthalpy F_E, radiative F_R, kinetic F_K, and total F_T energy fluxes. The total energy flux is the sum of the other three

$$F_T = F_E + F_K + F_R \quad . \tag{5}$$

A time average of these fluxes is shown here. The total flux at each depth is seen to be nearly equal to the imposed flux along the lower boundary, which is indicative of convective equilibrium. The enthalpy flux can be written in terms of a mass weighted correlation of the temperature and radial velocity fluctuations

$$F_E =< c_P \ \rho \ \delta T \ U_R > \tag{6}$$

The kinetic energy flux is related to a similar correlation between the radial velocity and velocity squared, which includes the independent transverse components of velocity,

$$F_K =< \frac{1}{2} \rho \ U^2 \ U_R > \tag{7}$$

The radiative flux can be written directly in terms of the average temperature gradient (weighted by the thermal diffusivity)

$$F_R = - < \chi \frac{\partial T}{\partial Z} > \quad . \tag{8}$$

A local MLT model for efficient convection can be formulated in terms of the correlations implicit in the equations above. We can define two correlation coefficients as functions of the vertical coordinate. One is related to the enthalpy flux

$$\alpha_E = \frac{< \rho \ \delta T \ U_R >}{< \rho >< \delta T^2 >^{1/2} < \delta U_R^2 >^{1/2}} \quad . \tag{9}$$

The other correlation coefficient is motivated by the kinetic energy flux

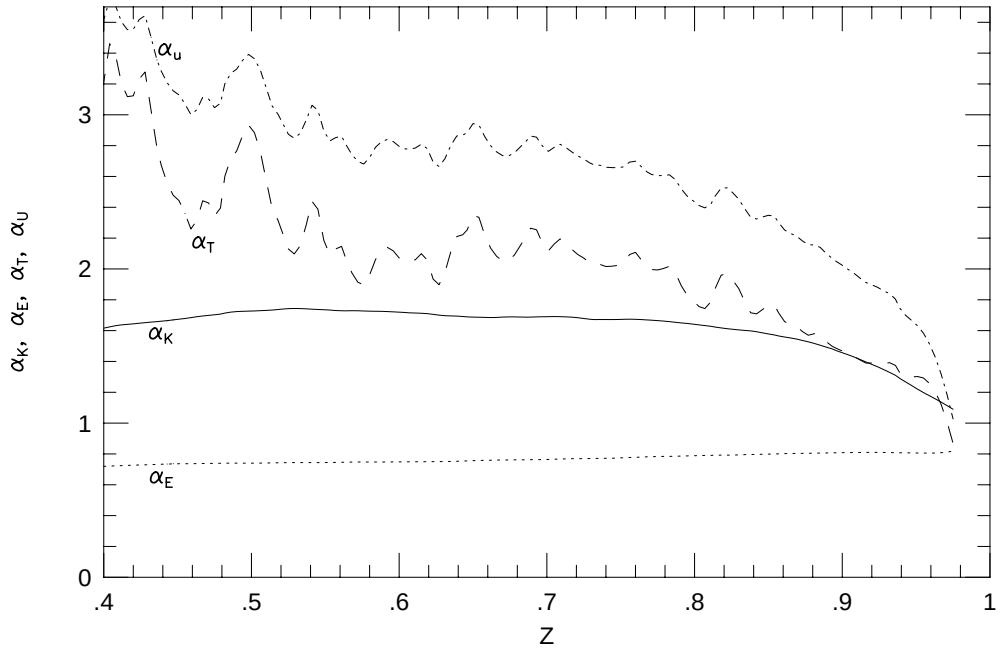

Figure 5. MLT correlation coefficients.

$$\alpha_K = \frac{< \rho\, U^2\, U_R >}{< \rho > < \delta U_R^2 >^{3/2}} \tag{10}$$

To the extent that α_E and α_K are constants independent of depth, imposed total flux, or other convective parameters, we can write the enthalpy and kinetic energy fluxes in terms of powers of the *rms* temperature and radial velocity fluctuations.

Both α_E and α_K are shown as functions of Z in Fig. 5. Both of these correlation coefficients are fairly constant for $Z \in (0.54, 0.89)$ which spans about two pressure scale heights in this model. A local MLT additionally relates the fluctuations of temperature and velocity to the degree to which the local temperature gradient is superadiabatic, and can be written in terms of two new coefficients for the temperature fluctuations

$$< \delta T^2 >^{1/2} = \alpha_T\ \Delta\nabla\ T \tag{11}$$

and the radial velocity fluctuations

$$< \delta U_R^2 >^{1/2} = \frac{\alpha_U}{2}\ \sqrt{\frac{\gamma - 1}{\gamma}}\ (\Delta\nabla)^{1/2} c \quad , \tag{12}$$

where

$$c = \sqrt{\gamma \frac{P}{\rho}} \quad , \qquad \Delta\nabla = \nabla - \nabla_{ad} \tag{13}$$

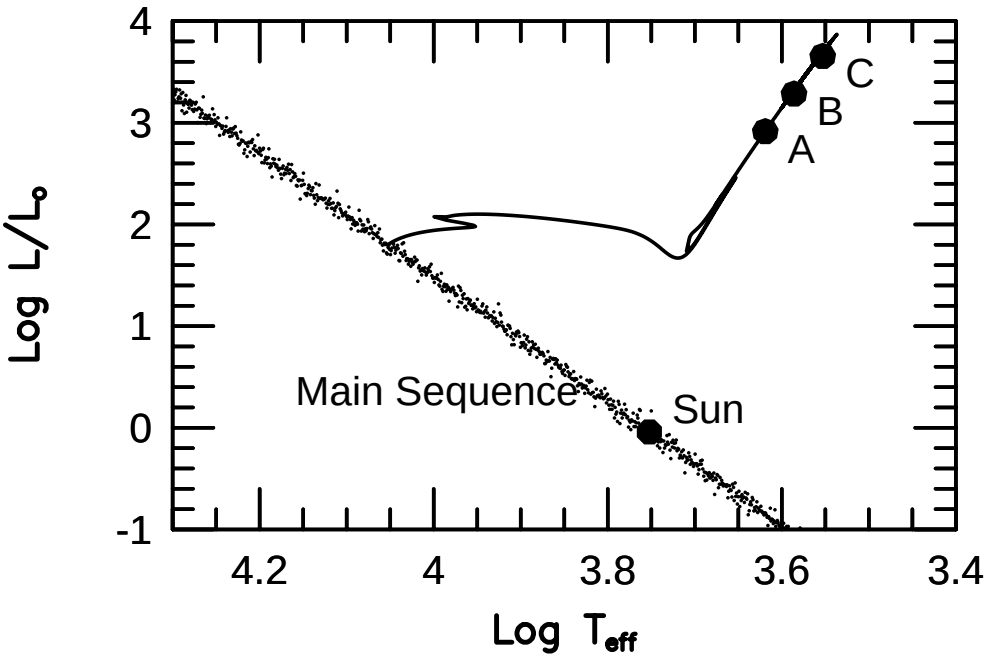

Figure 6. Evolutionary track of a three solar mass star (X=0.726, Y=0.254) with a schematic representation of the main sequence and solar parameters. Dots at A, B, and C represent where the star's thermal and mechanical properties match those of the models discussed here. Evolutionary track from S. Kawaler 1998

To the extent that α_T and α_U are constants one has a simple relation between the temperature gradient and the *rms* fluctuations of temperature and velocity. Fig. 5 also shows α_T and α_U as functions of Z. If all four alphas were constant, then the local temperature gradient could be related to the imposed flux and the local pressure, density, and gravity. These coefficients are nearly constant for $Z \in (0.54, 0.89)$ in this model of slab convection. These four coefficients are found to be independent of depth and have the same values here as in other models of convection in slab geometry with different convective energy flux (Porter and Woodward 2000).

3. Convection in Spheroidal Geometry

Numerical models of thermally driven convection in spheroidal geometry are used to examine the nature of turbulent efficient convection in radially deep convection zones, as are expected in red giant stars. Given the physical simplifications adopted in this present work (i.e., ideal gas, simplified radiative transport), there are three unitless numbers which specify the mechanical and thermal properties of the convection zone: ratio of envelope mass M_{env} to core mass M_{core}, ratio of thermal relaxation time τ_{thrm} to the acoustic time τ_{dyn}, and radial contrast across the convection zone R_{max}/R_{min}. Here, R_{min} corresponds to the radius of the impenetrable lower boundary used in the numerical models and, due to

limitations of mesh resolution, is a much larger fraction of star's total radius in these models than the lower boundary of the convection zone is in a typical red giant star. Correspondingly, M_{core} is the mass inside of R_{min} and represents a slightly larger faction of the star's mass than does the stable region in a red giant. These three ratios can be related to the mass and luminosity of a star on the RGB or AGB track via evolutionary models.

Acoustic and thermal relaxation time scales can be related to the mass and luminosity of a star via simple dimensional analysis. The thermal time can be written as

$$\tau_{thrm} = \frac{E_H}{L} \sim \frac{GM^2}{RL} \quad , \tag{14}$$

while the acoustic, or sound crossing, time is

$$\tau_{dyn} = \int \frac{dR}{c} \sim R^{3/2} M^{-1/2} \quad , \tag{15}$$

where E_H is the heat energy in the convective envelope of the star, L is the luminosity, G is the universal gravitational constant, M is the total mass, R is the radius, and c is the local speed of sound. Evolutionary models (Iben 1984) give us the scalings of radius and luminosity with mass and effective temperature

$$R \sim L^{0.68} M^{0.32} \tag{16}$$

$$L \sim M^{1.78} T_{eff}^{-11.1} \quad . \tag{17}$$

From these equations we get the scaling of luminosity with the ratio of the two time scales

$$L \sim (\frac{\tau_{thrm}}{\tau_{dyn}})^{-0.37} \tag{18}$$

A temperature vs. luminosity diagram, Fig. 6, with schematic representations of where the main sequence and the Sun lie, shows a three solar mass star's evolutionary track (Kawaler 1998) and three points in its asymptotic giant branch phase at which the mechanical and thermal parameters of the star's convective envelope most closely match those of the numerical models of convection discussed here. Dimensionless ratios for four simulations of convection in spheroidal geometry are listed in Table I.

Run	$\frac{M}{M_\odot}$	$\frac{L}{L_\odot}$	$\frac{M_{env}}{M_{core}}$	$\frac{\tau_{thrm}}{\tau_{dyn}}$	$\frac{R_{max}}{R_{min}}$
A	3.0	821	4.0	90,000	10
B	3.0	1,926	4.0	9,000	10
C	3.0	4,519	4.0	900	10
D	—	—	0.0035	193	6

Run D is an extreme case (i.e., negligible mass in the convective envelope) and is used here to test the robustness of the results. Runs C and D will be discussed here (runs A and B are still in progress).

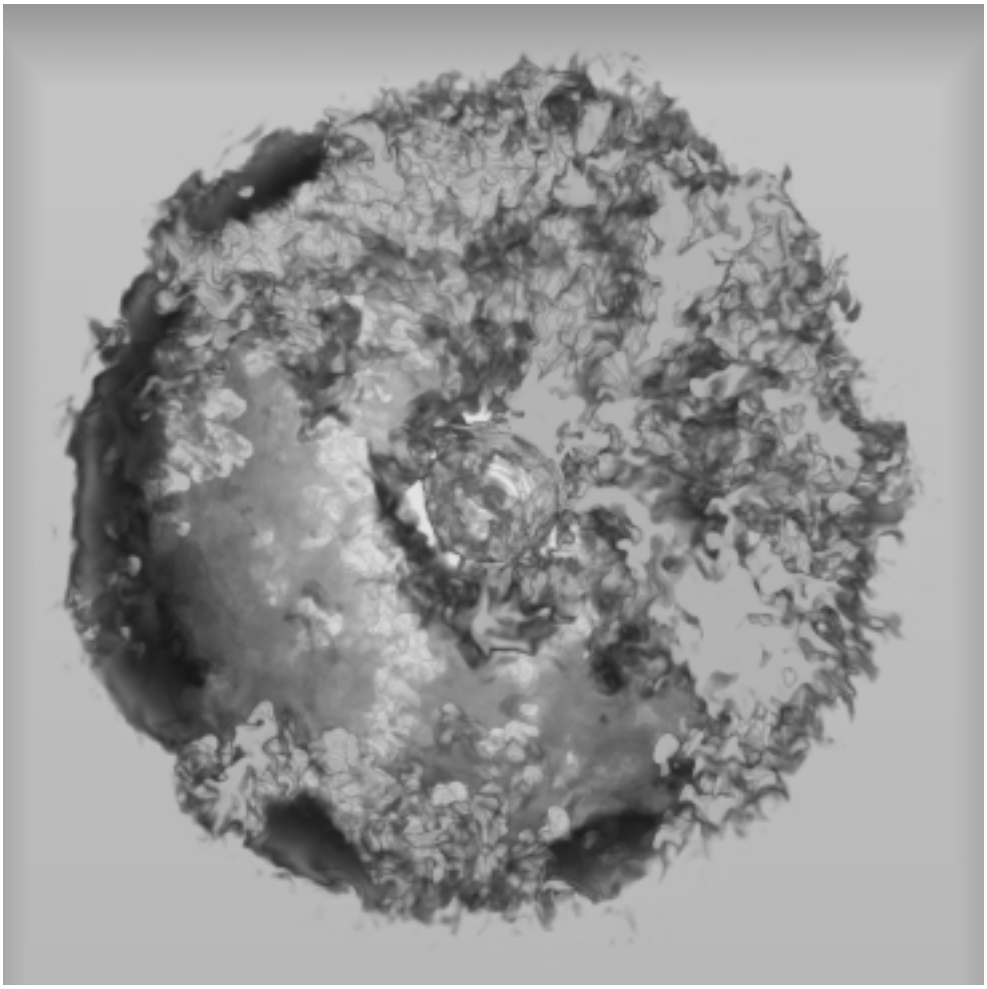

Figure 7. Temperature fluctuations from a simulation (run D in table I) of convection in spheroidal geometry.

Temperature fluctuations (dark gray = hot, light gray = cool) relative to the mean temperature for a given pressure are shown in a melon slice from run D in Fig 7. The predominance of cool fluctuations on the upper right suggests a dipole mode, which is also seen in the radial velocity (dark gray = downflow, light gray = upflow) in a thin section shown in Fig. 8.
We quantify the amplitude of the velocity fluctuations at a given radius by sampling the radial velocity on a sphere, Fig. 9, and extracting the amplitudes of the spherical harmonic modes. The spherical harmonic power spectrum of the radial velocity

$$E_l^U \;=\; \sum_m |\; \tilde{U}_{lm}|^2 \quad , \tag{19}$$

where

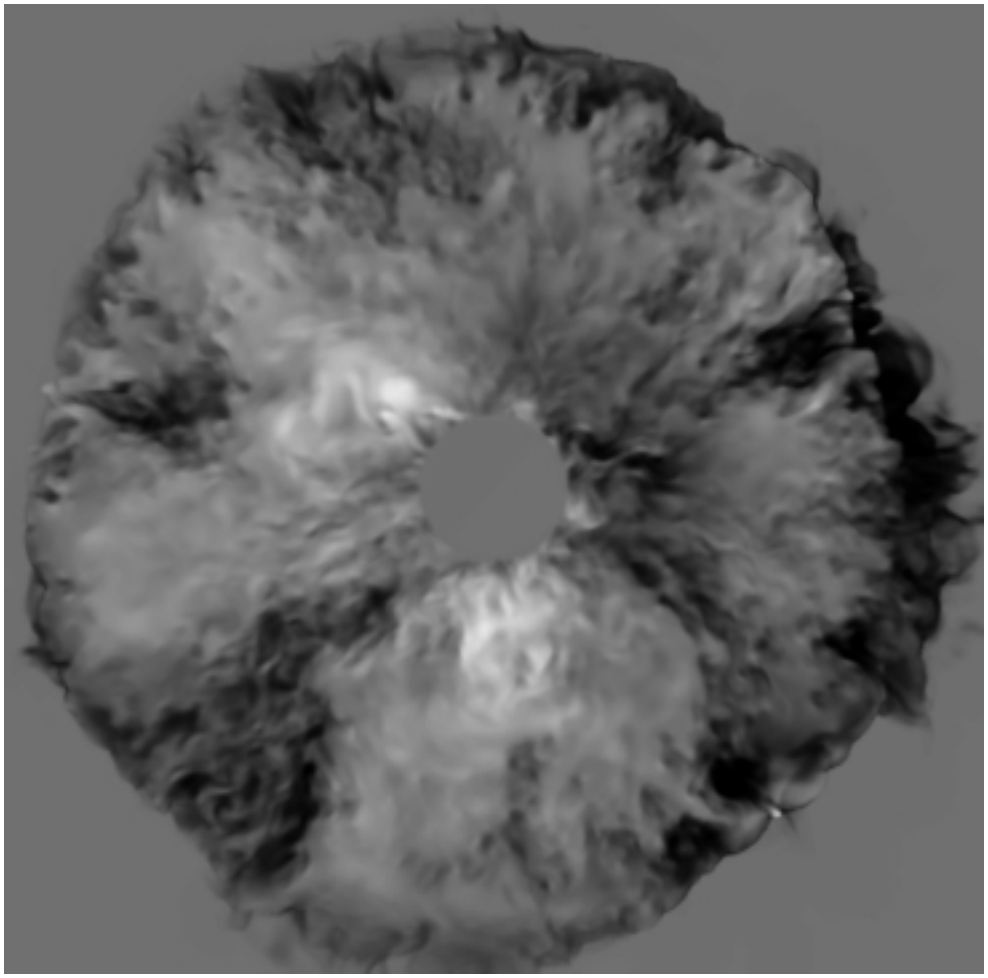

Figure 8. Radial velocity from run D (see table I) of convection in spheroidal geometry.

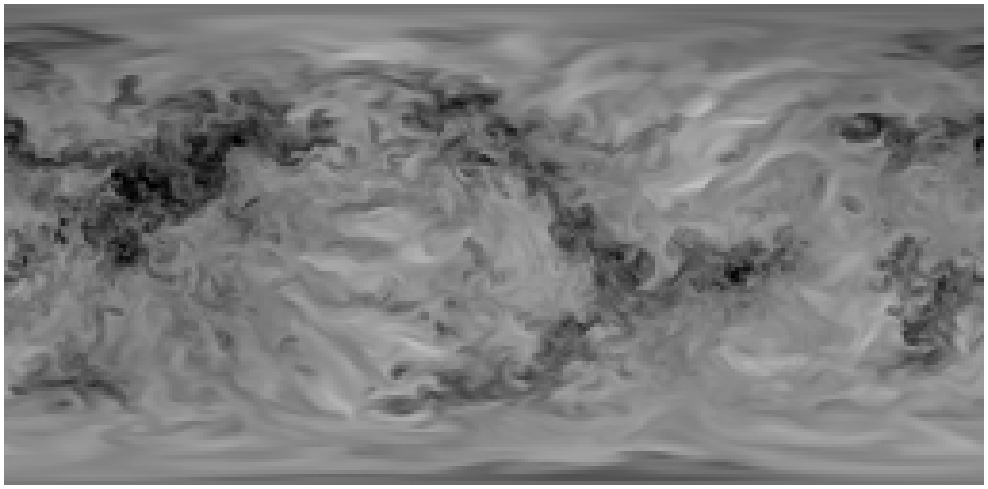

Figure 9. Radial velocity sampled on a sphere at $R = 0.5R_{max}$ from a simulation (D see table I) of convection in spheroidal geometry.

$$U_R \;=\; \sum_{lm} \tilde{U}_{lm}\, Y_{lm} \quad , \tag{20}$$

gives the energy at wave number

$$k = \frac{\sqrt{l(l+1)}}{R} \quad . \tag{21}$$

The radial velocity spectra from run D are shown for velocities sampled on spheres at three radii (20%, 40%, and 80% of R_{max}) in Fig. 10. Note that the dipole mode ($l = 1$) has the largest amplitude at all three radii. Just as with the slab convection simulations, the fundamental mode dominates the flow both in terms of an energy spectrum as well as the structures in configuration space seen in the visualizations. There is also, similar to slab convection simulations, a Kolmogorov-like range at radii equal to 20% and 40% of R_{max}, where the velocity spectra scale as $k^{-5/3}$. Just as in slab convection, the high wavenumber end of this $k^{-5/3}$ range can be understood in terms of the near dissipation range energy enhancement where, at wavelengths $\lambda < 32\Delta x$, there is excess of energy over what would be expected from the $k^{-5/3}$ scaling. In slab geometry, the spectrum of convective motions was found to be damped for wavelengths larger than twice the depth below the upper boundary (Porter and Woodward 2000). A similar rule seems to apply here. Between these two limits, shown as vertical lines in each of the three panels of Fig. 10, the velocity spectra are seen to scale in a Kolmogorov-like manner.

Run D is an extreme case of negligible mass in the convective envelope compared with that in the core. Run C is much more typical of a red giant star. The velocity spectra, shown in the left panel of Fig. 11 are from run C and are very similar to those of run D. The three sets of velocity spectra shown in Fig. 11 are from numerical models differing only in mesh resolution, all three share the mechanical properties of run C. The three mesh resolutions are 100, 200, and

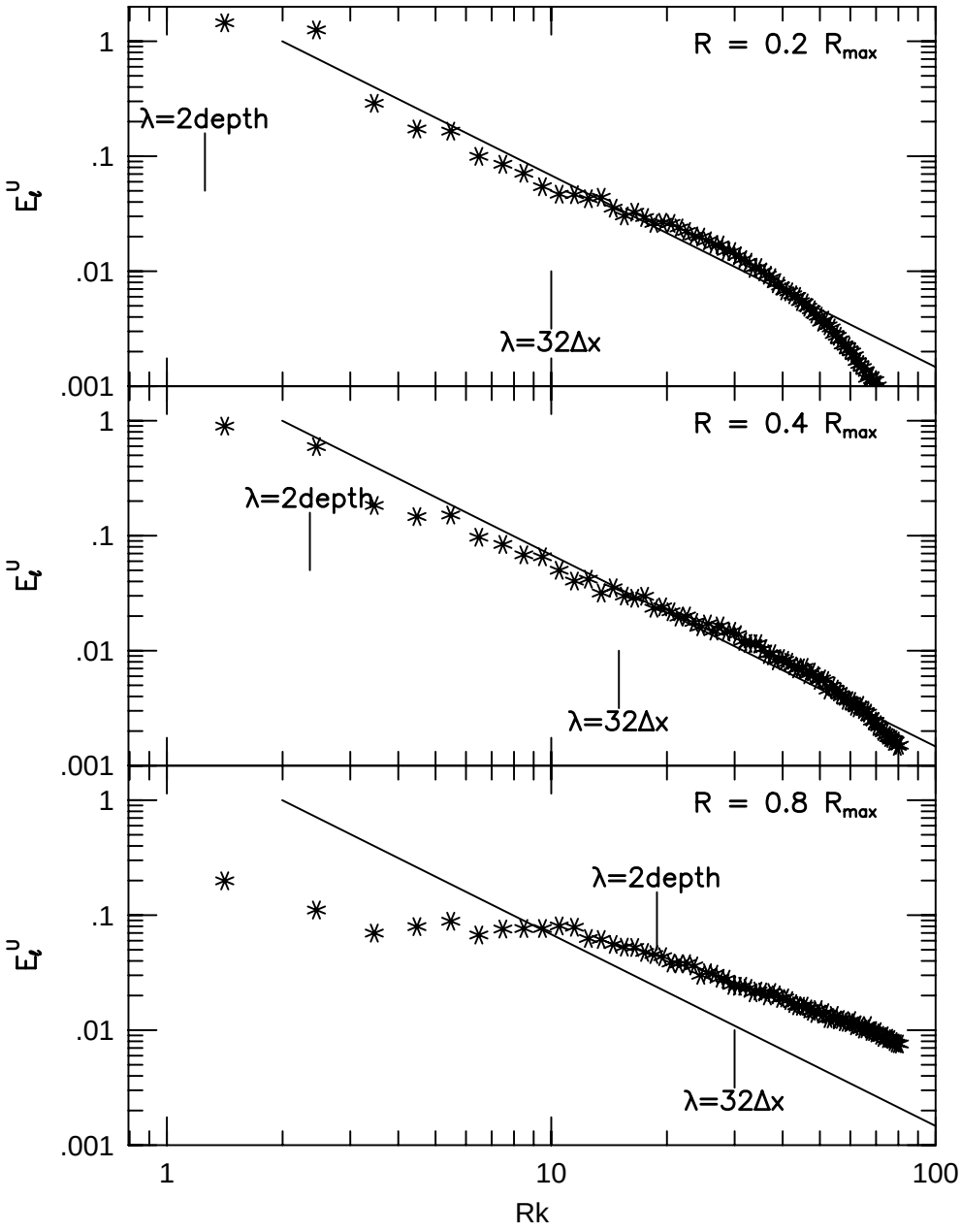

Figure 10. Radial velocity spectra taken at three radii in run D.

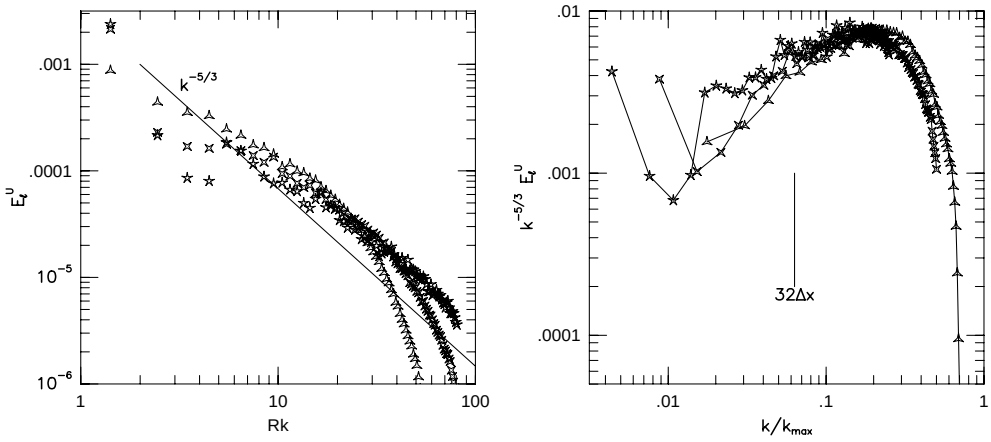

Figure 11. Velocity spectra (left panel) and compensated velocity spectra (right panel) taken at $R = 0.5R_{max}$ from simulations run on three numerical meshes, all simulations are run with run C parameters.

400 mesh cells across the diameter of the convection zone. In order of increasing mesh resolution these three runs are indicated by 3, 4, and 5 pointed stars. Note the agreement between the two highest resolutions for the $l = 1$ and $l = 2$ modes. The right panel of Fig. 11 shows compensated velocity spectra, from the same three simulations, which have been shifted to match their dissipation ranges. Indirect effects of the dissipation range are seen even in the $l = 1$ mode of the lowest resolution run here.

3.1. Radial Profiles in Spheroidal Geometry

Given hydrostatic equilibrium, the radial profiles of thermodynamic quantities depend on the temperature gradient. The temperature gradient is often given in terms of d ln T/d ln P. The radial profiles of d ln T/d ln P (solid line) and entropy (dashed line) for the three solar mass high luminosity case (run C) are shown in the left panel of Fig. 12. Vertical ticks represent pressure scale heights. Superadiabatic temperature gradients are seen for $R > 1.5$, while subadiabatic temperature gradients are seen for $R < 1.2$.

The total luminosity is carried primarily by the convective flux (sum of enthalpy L_E and kinetic L_K) in most of the convection zone of run C. These luminosities, shown in the right panel of Fig. 12, are scaled to the imposed luminosity. The convective flux is seen to be nearly constant, and equal to the imposed luminosity, from R=0.6 to R=2.8, indicative of convective equilibrium. As has been seen in slab convection, the kinetic flux is negative, and tends to increase in magnitude with depth.

The RMS radial velocity fluctuations (solid line in the left panel of Fig 13) are seen to decrease with depth, similar to slab convection, for $R > 2.3$. In both slab geometry and the outer radii of spheroidal geometry the velocity fluctuations are expected to decrease with depth because the total mass and heat capacity available to carry the convective flux increases with depth. However,the total mass in a radial interval depends not only on the mass density but also on the area, which decreases as the square of the radius in spheroidal geometry.

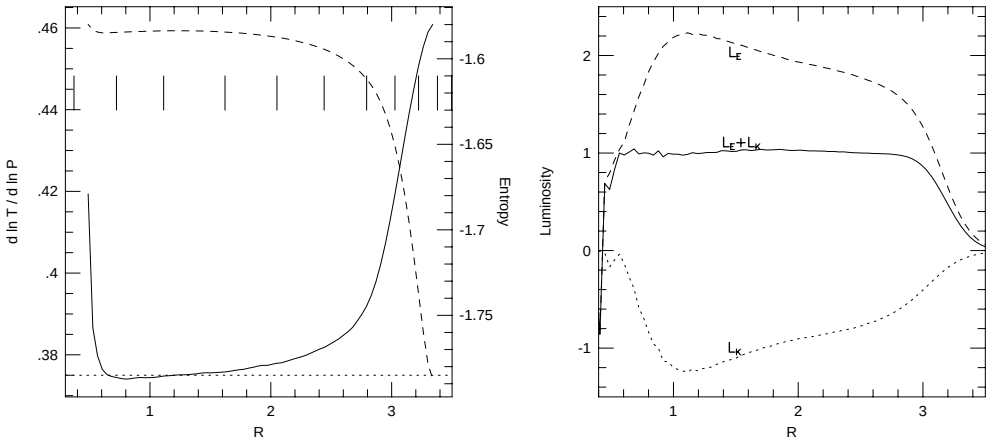

Figure 12. Temperature gradient and entropy (left) and kinetic luminosity, enthalpy luminosity, and their sum (right), as functions of radius, from run C.

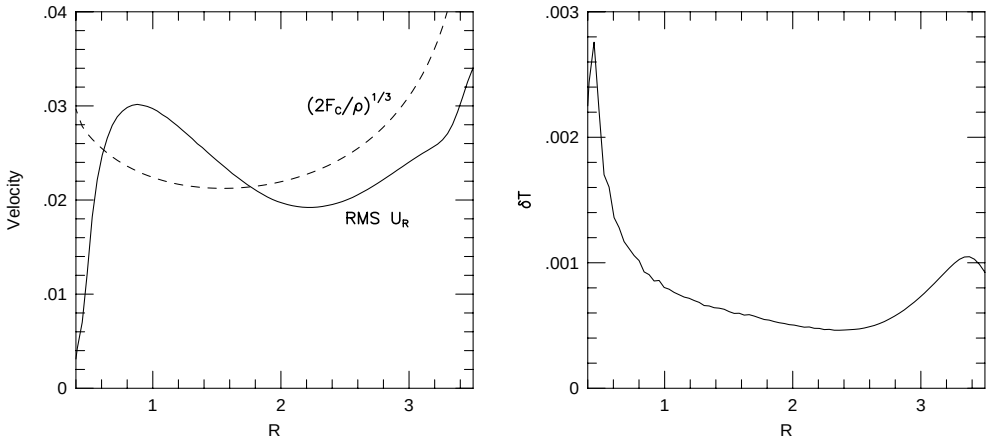

Figure 13. RMS Velocity fluctuations (left) and RMS temperature fluctuations (right), as functions of radius, from run C.

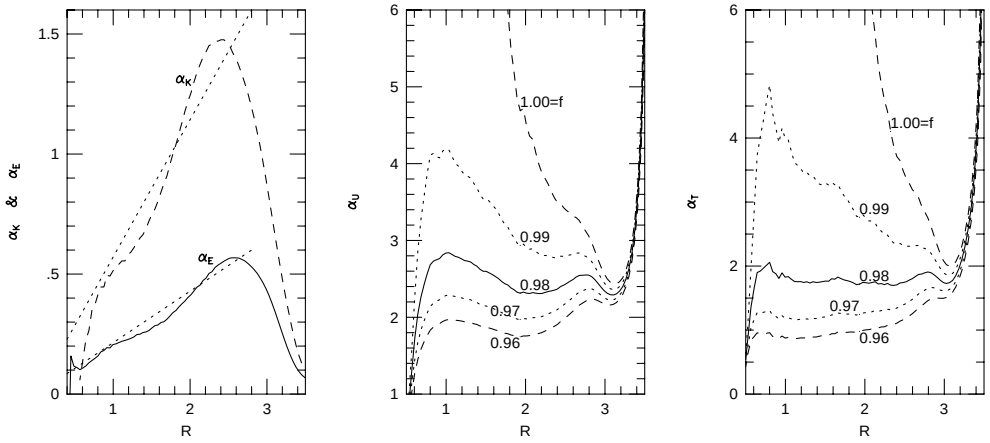

Figure 14. Enthalpy and kinetic flux correlation coefficients (left), velocity (middle) and temperature fluctuation (right) coefficients for convection in spheroidal geometry (run C).

A scaling argument relating a given luminosity to the amplitude of velocity fluctuations needs to take this area factor into account

$$\frac{L_C}{4\pi R^2} \;=\; F_C \;=\; \frac{1}{2}\rho U_R^3 \tag{22}$$

Here, for $R < 2$, velocity fluctuations increase with depth even faster than the area factor would predict. This added increase in velocity fluctuations with depth is a side effect of the coherent dipolar flow for $R < 2.3$ in this simulation.

RMS temperature fluctuations (shown in the right panel of Fig 13) also decrease with depth for $R > 2.3$, as in slab geometry, but increase with depth for $R < 2.1$

3.2. Local MLT in Spheroidal Geometry

We can define the same correlation functions for convection in spheroidal geometry as we did in slab geometry with the difference that the fluxes must be scaled by the surface area at each radius.

$$L_C = L_E + L_K \quad , \quad L_i = 4\pi R^2 F_i \tag{23}$$

$$F_E =< c_P\ \rho\ \delta T\ U_R >= \alpha_E < \rho >< \delta T^2 >^{1/2} < \delta U_R^2 >^{1/2} \tag{24}$$

$$F_K =< \frac{1}{2}\rho\ U^2\ U_R >= \frac{\alpha_K}{2} < \rho > < \delta U_R^2 >^{3/2} \tag{25}$$

The correlation coefficients α_E and α_K are shown as functions of radius in the left panel of Fig. 14. Unlike slab convection, the correlation coefficient of the velocity and temperature fluctuations, α_E, (solid line) is seen to scale almost linearly with the radius for $R < 2.3$ The correlation for the kinetic energy flux, α_K (dashed line), also scales nearly linearly with radius over the same

range of radii. The dipolar flow, seen in visualizations (Fig. 8) and measured in velocity spectra (Fig. 10 and Fig. 11), produces nearly uniform flow past the central core. The resulting near even symmetry of the temperature and kinetic energy fields coupled with the near odd symmetry of the radial velocity field leads to cancelation of a large part of both the enthalpy and kinetic energy fluxes. Apparently, the *fractional* cancelation becomes increasingly perfect as the center is approached. Of course, the net radial enthalpy and kinetic fluxs still integrate to the imposed luminosity (see Fig. 12). Further, near the center in a dipolar flow, fluid elements do not change direction in going from being part of a downflow to being part of an upflow as they pass the center. Hence, fluid elements need not break their momentum, as they would in slab geometry, and the same driving energy flux leads to larger velocity and temperature fluctuations than in slab geometry.

In relating velocity and temperature fluctuations to the temperature gradient we find that a much better fit is achieved if the adiabatic temperature gradient ∇_{ad} is adjusted by a factor of $f = 0.98$ (solid lines in the middle and right panels of Fig. 14 according to

$$< \delta U_R^2 >^{1/2} = \frac{\alpha_U}{2} \sqrt{\frac{\gamma - 1}{\gamma}} \, (\Delta_f \nabla)^{1/2} \, c \tag{26}$$

$$< \delta T^2 >^{1/2} = \alpha_T \, (\Delta_f \nabla) \, T \tag{27}$$

where

$$\Delta_f \nabla = \nabla - f \nabla_{ad} \tag{28}$$

Fig. 14, middle and right panels, show α_U and α_T for f ranging from 0.96 to 1.00 . Both alphas dramatically increase with depth for the unmodified value of ∇_{ad}, corresponding to $f = 1$. This leads to a subadiabatic temperature gradient within the convection zone, which has also been seen in models of convection in slab geometry (Sofia and Chan 1989, Cattaneo et. al. 1991, and Porter and Woodward 2000). Indeed, Sofia and Chan (1989) observed that the same adjustment factor ($f = 0.98$) worked best for the fit of the rms temperature fluctuations to the $\Delta\nabla$ factor. In all three simulations of slab convection, the subadiabatic region is geometrically in the lower half of the box, which is spanned by the lowest pressure scale height. Hence it was unclear whether the modification of ∇_{ad} needed for the local MLT fit was due to the impenetrable lower boundary condition or due to non-local effects. Unlike convection in slab geometry, however, in this model of spheroidal geometry the convection zone spans seven pressure scale heights, the subadiabatic temperature gradient spans two pressure scale heights and is at least one pressure scale height away from the impenetrable boundary at R_{min}. Non-local effects of coherent convective structures are evident in the statistics of spheroidal convection presented here.

4. Non-Local Convection

Convective motions can exist in a subadiabatic region, and even be buoyantly driven, because coherent convective motions span many pressure scale heights.

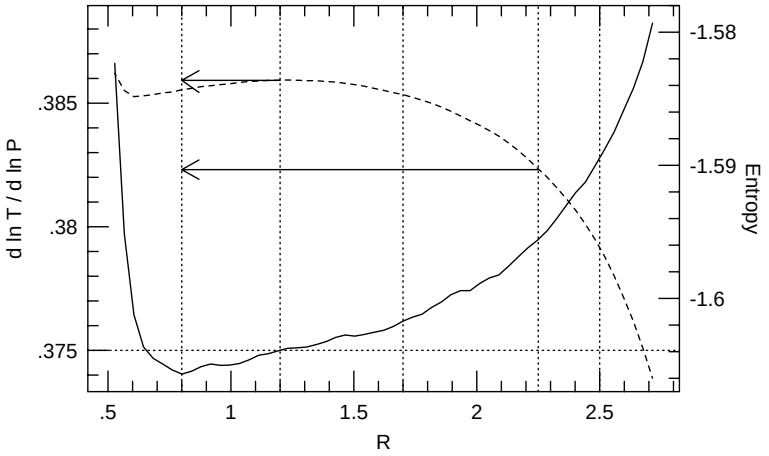

Figure 15. Detail of temperature gradient and entropy profiles from run C.

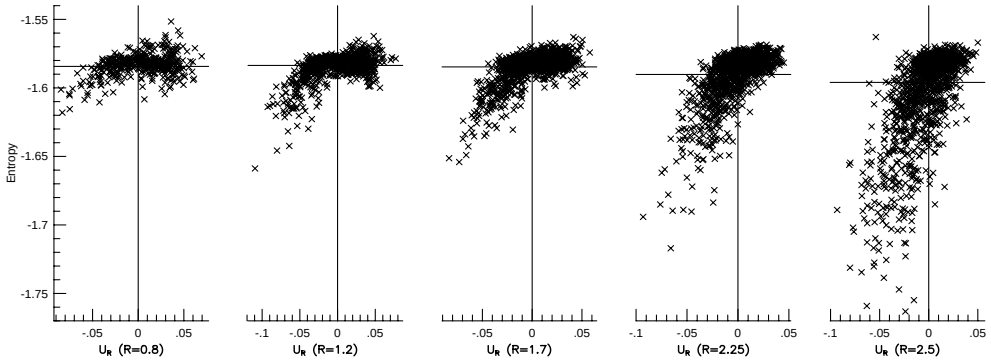

Figure 16. Entropy vs. radial velocity scatter plots for 5 radii from run C.

In both slab and spheroidal geometries, visualizations clearly show cool downflow plumes, as well as warm updrafts, spanning the entire vertical extent of the convection zone. These convective structures do not totally mix with the surrounding gas even after moving through several pressure scale heights. Further, the simulations described here are of efficient convection, so thermal diffusivity does not cause elements of gas to loose their thermal/buoyant identity before they move very far.

The temperature gradient and entropy profiles from run C are shown in Fig. 15. The horizontal dotted line indicates the adiabatic value of $dlnT/dlnP$ for this $\gamma = 1.6$ atmosphere. Assuming no mixing, no shocks, and no thermal diffusivity, an element of gas will retain its entropy. If such an element starts out neutrally buoyant, and the temperature gradient is subadiabatic over the entire course of the element's downward motion (upper arrow in Fig. 15), then the element will end up with a larger entropy than its surroundings and will be positively buoyant. However, if a similar element, starting with neutral buoyancy, moves into a subadiabatic region after traversing an extended superadiabatic

range of depths, then it may still be very negatively buoyant (lower arrow in Fig. 15).

Scatter plots of radial velocity vs. entropy taken at five radii, shown in Fig. 16, illustrate that something like the latter description is indeed going on in these simulations. The five radii are indicated by the vertical dotted lines in Fig. 15. Even at R=0.8 (the most subadiabatic region) entropy and radial velocity are positively correlated, indicative of buoyancy driving as well as a positive enthalpy flux (see also the enthalpy luminosity in Fig. 12). Comparison with the scatter plots at the other 4 radii (all plotted on the same entropy scale) show that there is plenty of room for a downflowing element of gas which starts at $R = 2.5$ to increase its entropy (mainly due to mixing in this example) and still be negatively buoyant by the time it reaches $R = 0.8$.

5. Conclusions

The simulations of efficient thermally driven convection discussed in this paper exhibit turbulent flows which are dominated by the fundamental (i.e. longest wavelength) modes. For convection in slab geometry, with 2x2x1 aspect ratio this leads to one convection cell filling the lowest pressure scale height across the horizontal span of the box. Hence, the periodic boundary conditions in those simulations had a significant effect on the largest scale of the flow. In spheroidal geometry a dipolar flow spans most of the convection zone. The fluid turbulence in these simulations spans a wide range of interacting scales. The velocity spectrum of the flows in both geometries has Kolmogorov-like $k^{-5/3}$ scaling.

The efficient convection in these simulations establishes a nearly adiabatic radial profile. Both geometries generate a subadiabatic region which, in spheroidal geometry models, is clearly identifiable with non-local effects. In slab geometry, well away from the vertical impenetrable boundaries, scaling of the vertical energy fluxes with the temperature and velocity fluctuations are consistent with simple local MLT. By contrast, in spheroidal geometry the correlation coefficients of the temperature and velocity fluctuations scale nearly linearly with the radius.

These simulations of convection in spheroidal geometry are the first in a series of studies which seeks to investigate the nature of convection in deep convective envelopes such as those found in red giant stars. The highly idealized microphysics used in the spheroidal simulations here (i.e., ideal gas laws, constant or negligible thermal diffusivity, and a simple cooling law for the photosphere) was chosen to simplify the interpretation in this preliminary work, and to allow direct comparisons with previous simulations done in slab geometry. Variable equation of state and variable thermal diffusivity have already been implemented and tested in the PPM hydrodynamics code. Table look-ups for astrophysically relevant microphysics along with an improved photospheric boundary condition are currently being implemented and tested. With these improvements, 3D turbulent numerical models of convection in spheroidal geometry should be able to address issues such as the role convection plays in driving and damping radial pulsations, as well as the distribution of temperature and velocity variations near the surface, in radially deep convective envelopes. Comparisons could then

be made with observation of light curves, line broadening, and the possible existence of star spots in red giant stars.

Acknowledgments. We would like to thank J. Robert Buchler for inviting dhp to a very interesting and productive work shop. We are pleased to acknowledge NSF grants of computer time at PSC and NCSA, as well as a grant of computer time at the Minnesota Supercomputer Institute at the University of Minnesota. Visualization and analysis of these simulations was performed in the Laboratory for Computational Science and Engineering at the University of Minnesota. This work was supported by the National Science Foundation, through grand challenge grant ASC-9217394, and by NASA through grant USRA/5555-23/NASA.

References

Asida, S. M., and Tuchman, Y. 1997, Ap. J. 491, p. 147

Asida, S. M., 2000, "Calibrating the Mixing Length Parameter for a Red Giant envelope", to be published by Ap. J.

Cattaneo, F., Brummell, N.H., Toomre, J., Malagoli, A., Hurlburt, N. E., 1991 Ap. J. 370, pp. 282-294

Chan, K. L., and Sofia, S. 1989, Ap. J. 336 pp. 1022-1040

Chan, K. L., and Sofia, S. 1996, Ap. J. 466 pp. 372-383

Colella, P., and Woodward, P. R., 1984, J. Comput. Phys. 54, p. 174

Kawaler, S. 1998, private communication

Kim, Y.-C., Fox, P., Demarque, P., and Sofia, S. 1996, Ap. J. 461 pp. 499-506

Porter, D. H., Pouquet, A.,, and Woodward, P. R. 1994, Physics of Fluids A, 6, No. 6, pp. 2133-2142

Porter, D. H., and Woodward, P. R. 2000, In Press, to appear Ap. J. Suppl., March 2000 Vol. 127 no. 1

Singh, H. P., and Chan, K. L 1993, A & A 279 pp. 107-118

Sytine, I. V, Porter, D. H., Woodward, P. R., Hodson, S. H., and Winkler, K.-H., 1999, "Convergence Tests for Piecewise Parabolic Method and Navier-Stokes Solutions for Homogeneous Compressible Turbulence," Submitted to J. Comput. Phys., also UMSI 98/169 Oct 1998

Lohse, D., and A. Muller-Groeling, "Bottleneck effects in turbulence: Scaling phenomena in r versus p space", Phys. Rev. Lett. 74, 1747 1995

Iben, I. 1984, Ap. J. 227, pp. 333-354

Woodward, P. R., and Colella, P., 1984, J. Comput. Phys., 54, p. 115

Woodward, P. R. 1986, in Astrophysical Radiation Hydrodynamics, ed. K.-H. Winkler & M. L. Norman (Dordrecht: Reidel), p. 245